

## Highlights

### **Using Machine Learning to Reduce Observational Biases When Detecting New Impacts on Mars**

Kiri L. Wagstaff, Ingrid J. Daubar, Gary Doran, Michael J. Munje, Valentin T. Bickel, Annabelle Gao, Joe Pate, Daniel Wexler

- Machine learning classifiers can help increase the detection of rare fresh impacts on Mars.
- The most-confident machine learning candidates preserve observational biases in the manually identified training examples.
- Analyzing candidates partitioned by thermal inertia bins reduces observational bias.

# Using Machine Learning to Reduce Observational Biases When Detecting New Impacts on Mars

Kiri L. Wagstaff<sup>a,\*</sup>, Ingrid J. Daubar<sup>b</sup>, Gary Doran<sup>a</sup>, Michael J. Munje<sup>a</sup>, Valentin T. Bickel<sup>c</sup>, Annabelle Gao<sup>b</sup>, Joe Pate<sup>b</sup> and Daniel Wexler<sup>b</sup>

<sup>a</sup>*Jet Propulsion Laboratory, California Institute of Technology, 4800 Oak Grove Drive, Pasadena, CA, 91109, USA*

<sup>b</sup>*Brown University, Earth, Environmental, and Planetary Science, Providence, RI, 02912, USA*

<sup>c</sup>*ETH Zurich, Engineering Geology, Zurich, 8092, CH*

---

## ARTICLE INFO

### Keywords:

Mars, surface  
Impact processes  
Cratering  
Image processing  
Experimental techniques

## ABSTRACT

The current inventory of recent (fresh) impacts on Mars shows a strong bias towards areas of low thermal inertia. These areas are generally visually bright, and impacts create dark scours and rays that make them easier to detect. It is expected that impacts occur at a similar rate in areas of higher thermal inertia, but those impacts are under-detected. This study investigates the use of a trained machine learning classifier to increase the detection of fresh impacts on Mars using CTX data. This approach discovered 69 new fresh impacts that have been confirmed with follow-up HiRISE images. We found that examining candidates partitioned by thermal inertia (TI) values, which is only possible due to the large number of machine learning candidates, helps reduce the observational bias and increase the number of known high-TI impacts.

---

## 1. Introduction

New impact craters continue to appear on the surface of Mars. The steadily growing body of observational data acquired by orbital instruments has enabled the confident identification of more than a thousand dated recent (“fresh”) impacts, which are defined as craters that are constrained by images of the same area before and after the impact occurred. Newly forming craters were first discovered on Mars by Malin et al. (2006), who performed an imaging campaign with the Mars Global Surveyor Mars Orbiter Camera (MOC) to find twenty new impacts by manually comparing repeat images of the same areas. These techniques have continued with the Context Camera (CTX) (Malin et al., 2007) on the Mars Reconnaissance Orbiter for the last ~15 years (Daubar et al., 2013, 2022). Newly acquired CTX images are manually searched for distinctive features resembling past discoveries of new impacts, and then previous imagery from various orbiters is compared to find the most recent image in which the feature was absent. If one is found, a follow-up high-resolution image is requested from the High Resolution Imaging Science Experiment (HiRISE) on MRO (McEwen et al., 2007). These new craters have been rich sources of new information about Mars, for example studies of subsurface ice exposures (Byrne et al., 2009; Dundas et al., 2014, 2021) and mineralogy (Viviano et al., 2019), statistics (Daubar et al., 2013; Williams et al., 2014; Hartmann and Daubar, 2017; Daubar et al., 2019) and morphology (Daubar et al., 2014) of current martian cratering, and investigations of the dust-related albedo features around the new craters (Burleigh et al., 2012; Daubar et al., 2016; Bart et al., 2019).

One perplexing aspect of the current inventory of known fresh impacts on Mars (Daubar et al., 2022) is that their properties are not consistent with the global properties of Mars. For example, Figure 1 compares the distribution of thermal inertia values for known fresh impacts versus the rest of Mars. Thermal inertia characterizes the ability of a material to store and retain heat. High thermal inertia on Mars corresponds to rocky terrain, while low thermal inertia corresponds to dusty areas. In this figure, known impact craters within 60 degrees of the equator are binned by thermal inertia values derived from the Thermal Emission Imaging System (THEMIS) (Christensen et al., 2004) thermal inertia map (Edwards et al., 2011), using the Thermal Emission Spectrometer (TES) (Christensen et al., 2001) thermal inertia values (Putzig and Mellon, 2007) for regions where the THEMIS values are unavailable. Stacked bars show a breakdown of the impacts by appearance in comparison to the overall distribution of surface area by thermal

---

\*Corresponding author

 [kiri.wagstaff@jpl.nasa.gov](mailto:kiri.wagstaff@jpl.nasa.gov) (K.L. Wagstaff)

 <https://www.wkiri.com/> (K.L. Wagstaff)

ORCID(s): 0000-0003-4401-5506 (K.L. Wagstaff)

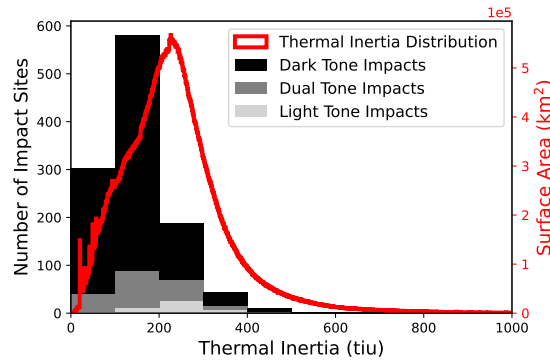


**Figure 1:** Thermal inertia distribution for fresh impacts from Daubar et al. (2022) within  $-60$  to  $60$  degrees latitude (histogram) compared with the overall thermal inertia distribution for Mars (red curve) over the same area, derived from TES and THEMIS thermal inertia maps. The stacked histogram shows detections by type. The thermal inertia values for fresh impact sites tends lower than that of Mars as a whole (peak near 150 tiu vs. 225 tiu).

inertia, similarly derived from the TES and THEMIS maps. The known population of fresh impacts shows a decided bias towards areas of lower thermal inertia. These regions are often visually bright due to sandy or dusty composition, and fresh impacts often create dark scour marks and rays that stand out to the human eye. It is expected that impacts are also occurring at the same rate in darker areas with higher thermal inertia, but to date they are under-represented in the inventory of known impacts. Effectively, rather than cataloguing all fresh impacts on Mars, existing detection efforts have dominantly identified dark-on-bright impacts that occur in areas of relatively low thermal inertia. This unintentional observational bias limits knowledge of the true impact cratering rate and affects analyses that rely on crater activity, such as estimating surface age (Hartmann and Neukum, 2001; Ivanov, 2001; Hartmann, 2005). As one possible adverse result, under-counting impacts in high thermal inertia areas could lead to a cratering chronology that over-estimates surface ages.

The goal of this work is to explore methods for correcting or reducing this bias to provide a more complete inventory of fresh impacts on Mars. There are many reasons why impacts in high thermal inertia (TI) areas could be overlooked, including their different appearance (often bright-on-dark instead of dark-on-bright), smaller or missing blast rays, or human oversight or fatigue. We hypothesize that training a machine learning classifier on known examples of low-TI and high-TI impacts could help improve consistency in detection and coverage of all impacts.

The contributions of this paper are (1) the addition of 69 impacts to the current inventory of confirmed fresh impacts on Mars, with five more waiting for HiRISE imaging, (2) characterization of key differences in detections found by humans versus those found by a machine learning algorithm, (3) reduction in observational bias achieved by separately analyzing detections from different thermal inertia settings, and (4) discussion of the implications of these findings for the use of machine learning to aid efforts to catalog features of interest on Mars and other planetary surfaces. Section 2 describes related work and the methods used in this study, Section 3 presents and analyzes the results, and conclusions are summarized in Section 4. An important lesson from this study is that the highest-confidence candidates found via machine learning exhibited the same observational bias inherent in the existing catalog, but the large number of candidates found globally enabled an analysis by thermal inertia value that reduced this bias.

## 2. Methods: Detecting fresh impacts with machine learning

Machine learning methods are increasingly employed to assist in the analysis of remote sensing data for planetary science and exploration. Examples include the classification of lunar soils using reflectance spectra (Kodikara and McHenry, 2020), the classification of terrain types in Mars orbital images to inform landing site selection (Ono et al., 2016; Barrett et al., 2022), the classification of rover and orbital images to enable content-based search of the Planetary Data System image archives (Wagstaff et al., 2018, 2021) or map features such as volcanic rootless cones and transverse aeolian ridges (Palafox et al., 2017) and rockfalls on Mars (Bickel et al., 2020b) and the Moon (Bickel et al., 2020a), and the identification of novel features in rover images to accelerate discovery (Kerner et al., 2020).

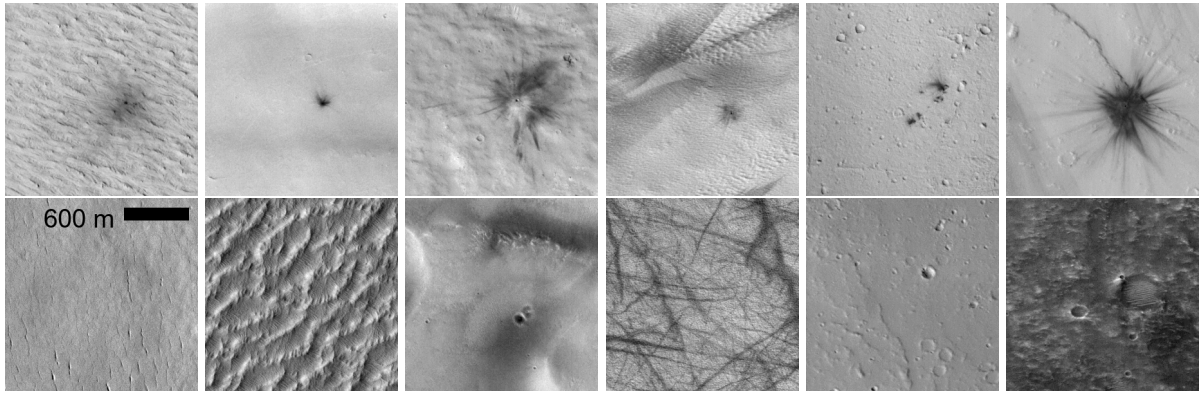


**Figure 2:** Examples of positive (top row) and negative (bottom row) CTX windows used to train the classifier to detect fresh impacts. CTX image credits: NASA/JPL/MSSS.

The current study investigates whether machine learning can also be effective in detecting fresh impacts in CTX images with the goal of increasing coverage and reducing observational bias in the catalog. Several previous investigations have employed machine learning methods to identify large craters; see DeLatta et al. (2019) for a historical overview and discussion of key issues. Silburt et al. (2019) trained a U-Net convolutional neural network (CNN) to detect craters in lunar digital elevation map images at a resolution of 118 m/pixel, and Jia et al. (2021) improved the U-Net’s performance with an attention-aware model. Wilhelm et al. (2020) labeled over 16,000 CTX image cutouts into 15 geomorphic surface classes, including “crater,” then compared the classification performance of six convolutional neural networks. Lagain et al. (2021) adapted a CNN that was trained on large craters in THEMIS data to apply to smaller craters in CTX images and used it to determine crater populations and infer the age of the ejecta blankets of ten large craters on Mars. However, none of these classifiers were trained to detect fresh impacts, which differ visually from the “crater” class in that fresh impacts often have scour marks and rays and may be so small that the crater itself is not resolved.

### 2.1. Training and evaluation of the machine learning classifier

We trained a convolutional neural network to classify CTX sub-images (windows) as containing a fresh impact or not. The windows are small sections of CTX source images that span  $300 \times 300$  pixels ( $\sim 1.8 \times 1.8$  km). This size was chosen to allow the detection of fresh impacts on the scale of a few hundred meters while including some surrounding context. We constructed a training set using an existing catalog of date-constrained fresh impacts that have confirmation from a HiRISE follow-up image (Daubar et al., 2013, 2020, 2022). We did not use examples from crater databases such as that of (Robbins and Hynek, 2012) to train the fresh impact classifier due to (1) the enormous difference in scale (e.g., the Robbins database contains craters larger than 1 km in diameter, but most fresh impacts are only a few meters in diameter) and (2) fresh impacts are primarily visible due to the surrounding albedo pattern; the craters themselves are not generally resolved. For these reasons, training on larger craters, which have a very different visual appearance, would likely be detrimental to the search for fresh impacts. Positive examples were centered on the location of a known fresh impact. We manually reviewed each such CTX image to exclude those that pre-dated the impact’s appearance or did not include the impact due to fading over time or poor localization. Negative examples were obtained from a spatially uniform random sampling of CTX images across the surface of Mars. In all, we obtained 1856 positive and 4973 negative images (total  $n = 6829$ ); examples are shown in Figure 2, and the full data set can be downloaded at <https://zenodo.org/record/5523886>.

We randomly separated the CTX images into 90% training ( $n = 6156$ ) and 10% held-out data ( $n = 673$ ). We increased the number of training examples by applying standard image augmentation techniques to modify the image without changing its class. Each training image was flipped horizontally and vertically; rotated by a random choice of 90, 180, or 270 degrees; adjusted by a minor (random) change to brightness, contrast, saturation, and hue; and blurred with a Gaussian filter with radius 2. In total, we employed 36,936 images (10,080 positive and 26,856 negative) images to train the classifier.

We used the state-of-the-art Inception-V3 image classifier (Szegedy et al., 2015), which was originally trained on 1.2 million images from the ImageNet data set (Russakovsky et al., 2015). CNN classifiers do not require the pre-specification of relevant features and instead automatically identify image properties that correlate with the classes of interest. We adapted Inception-V3 to classify fresh impacts in CTX images by performing additional training (“fine-tuning”) using the positive and negative CTX examples. The fine-tuning approach is generally more effective than training a randomly initialized neural network from scratch, since the pre-trained network has already learned general image properties from the much larger original data set. Inception-V3 employs 42 processing layers that include efficiency improvements to reduce the number of weights required and therefore the training time. To fine-tune this model for fresh impact detection, we used the PyTorch library (Paszke et al., 2019) with the Adam optimizer and cross entropy loss function. Other parameters include a starting learning rate of  $4 \times 10^{-6}$  with a decay of 0.1 every 10 steps, batch size of 32, and 25 epochs of training. The held-out set was used to calibrate the classifier’s predictions (posterior probability of a fresh impact) using bias-corrected temperature scaling (Alexandari et al., 2020). Calibration compensates for classifier over- or under-confidence by adjusting (rescaling) the output class probabilities so that they correspond to true occurrence rates in the held-out data set. The calculated scaling parameter (temperature) was 1.51 with class bias terms of  $-0.05$  (negative, non-impact) and  $0.26$  (positive, fresh impact). The calibration process reduced the Expected Calibration Error (Naeini et al., 2015) from 0.017 to 0.009 in the posterior probability values. The classifier achieved an accuracy of 97.5% (with precision 0.98, recall 0.93, and F1-score 0.95) on the held-out data set.

## 2.2. Deployment of machine learning classifier to the CTX archive

We deployed the trained classifier on the entire CTX archive, excluding images from the Mars Orbit Insertion and Cruise phases of the mission, as well as a few observations that caused issues because they were lacked valid geolocation information (e.g., calibration images). The resulting set contained 112,207 observations acquired between September 27, 2006 and December 1, 2019. We used the Gattaca supercomputer at JPL to process the observations in parallel using between 500 and 750 CPU cores over a period of about one week. Each observation was split into overlapping square windows 300 pixels in size, sliding 75 pixels at a time in each direction. The classifier was evaluated on each window, for a total of approximately 2 billion individual classifications. The total computation time across all cores was roughly 12 CPU-years.

After generating classification posterior probabilities with the classifier for each window, the full set of classifications was ranked in descending order of the probability that a fresh impact was present. Within the CTX archive, there may be multiple observations of the same location obtained at different times. Therefore, for each classification in the descending list, we grouped other windows that were found within 600 m of the classified window into a single “candidate” for manual inspection. Each window is associated with only a single candidate to avoid duplication.

The list of candidates was filtered for further analysis. First, informed by previous studies (Dundas et al., 2014; Daubar et al., 2016), we only considered candidates within the latitude range from  $-60$  to  $60$  degrees. High-latitude impact craters disappear quickly due to seasonal processes, and there is a lack of reliable training examples due to their rarity, seasonally poor illumination conditions, and seasonal changes in surface appearance due to ice and frost. Furthermore, we filtered out high-probability candidates for which there was not a least one non-detection (an overlapping window with a classification score below 0.5) within the candidate set that was acquired earlier. This excludes candidates for which the CTX data likely does not contain sufficient temporal coverage of the impact location to constrain its date of formation (i.e., an image the pre-dates the impact). After the filters were applied, a list of the 1000 highest-confidence candidates was generated for review.

## 2.3. Manual review of machine learning candidates

We performed a manual review of the top 1000 candidates identified by the classifier. The candidates were ranked in descending order of posterior probability as reported by the classifier; more than one million candidates had probability  $\geq 0.99$ . To facilitate this process, we generated a web page that provided information for each candidate, including all images of the candidate site (including repeat CTX observations, if available). We included only candidates whose first CTX observation was a non-detection (negative) to allow us to constrain the time of formation. Reviewing the complete time series of the location helps determine whether it is a valid fresh impact. Figure 3 shows an example candidate that consists of three CTX observations of the same location. Observations in which the classifier predicts a fresh impact probability of at least 0.95 are automatically outlined in green. The first observation does not contain an impact and was given a probability of 0.0, indicating that this impact occurred between January 19, 2015 and November 17, 2016.

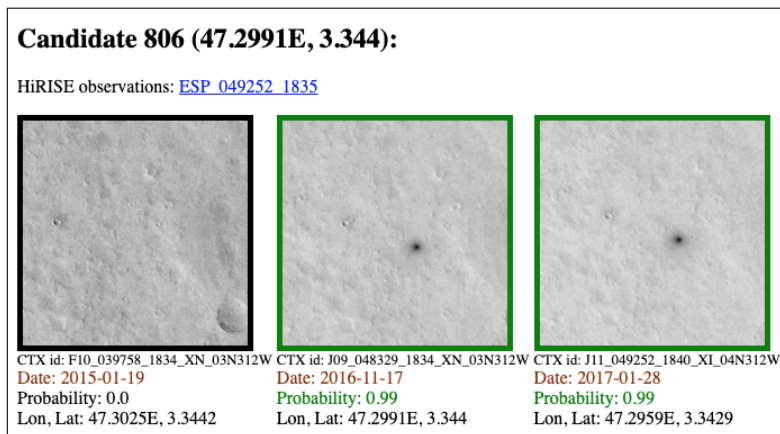


**Figure 3:** Information displayed for a fresh impact candidate found by the machine learning classifier to enable manual review. This candidate consisted of three CTX observations (the images are map-projected with north up). A link to any pre-existing HiRISE observations of the same area is provided to enable a high-resolution view when available and to facilitate identification of previously known fresh impact sites that had already been imaged by HiRISE. Note that since windows were independently generated by stepping every 75 pixels through different source CTX images, they are not perfectly registered. CTX image credits: NASA/JPL/MSSS.

The review page also includes a link to any overlapping HiRISE observation(s) that may already exist, enabling the reviewer to easily check for the presence of the impact at the time the HiRISE observation was collected.

The review process for each candidate proceeded as follows. Reviewers first examined the set of detection images for any newly appearing albedo features. In some cases, the classifier mistakenly assigned high probability to features that are not impacts, such as shadows from surface topography, dust devil tracks, wind or slope streaks, or other surface changes. Reviewers classified any such incorrect detections as “non-impact.” Impacts that appeared to be old and could not be date-constrained with a CTX image of the same location lacking the feature were designed “old impact.” Otherwise, reviewers checked for the earliest non-detection to constrain the date of formation. This enables us to determine with confidence that the feature is a “fresh” impact (occurred within the CTX operational period). If no preceding non-detection was available, but the albedo feature resembled a fresh impact blast zone, reviewers classified the candidate as an “undateable fresh impact.” Dateable fresh impacts were further divided into “known fresh impact” (already in the catalog) or “new fresh impact” (not previously known). In some cases, the classifier generated duplicate candidates from different observation dates that were not grouped due to localization errors. Reviewers marked these as “duplicate.” Reviewers also added other notes to aid interpretation where useful. Four reviewers contributed to the assessment of the top 1000 candidates to split up the work. At the beginning of the review process, all reviewers examined the same set of roughly 50 candidates, and any disagreements were discussed and resolved to ensure consistent evaluation of the remaining candidates.

For each candidate that was marked as “new fresh impact” (not previously known), we entered HiWish requests (<https://www.uahirise.org/hiwish/>; Chojnacki et al. (2020)) to obtain a high-resolution view of the same location for confirmation of the presence of an impact and measurements of crater characteristics. These targets were acquired by HiRISE between October 2020 and December 2021, resulting in 0.25 m/px images of each site.

## 2.4. Measurements of fresh impact features

To examine the ML-detected new impacts in the context of the broader human-detected catalog presented by Daubar et al. (2022), the same characteristics were measured for each ML-detected impact site. Specifically, we examined the follow-up HiRISE images of promising impact sites to catalog their features, including whether they contained a single crater or cluster of craters. We also characterized the albedo pattern around the impact site (diffuse halo, linear or arcuate rays, dark-, light- or dual-toned blast zone in comparison to the surroundings). Crater diameters were measured following the methodology of Daubar et al. (2013, 2019, 2022), using the CraterTools add-in for the Java Mission-planning and Analysis for Remote Sensing, JMARS (Christensen et al., 2009). For impacts that consisted of crater clusters, the individual diameters of the craters in the cluster were combined into an effective diameter that

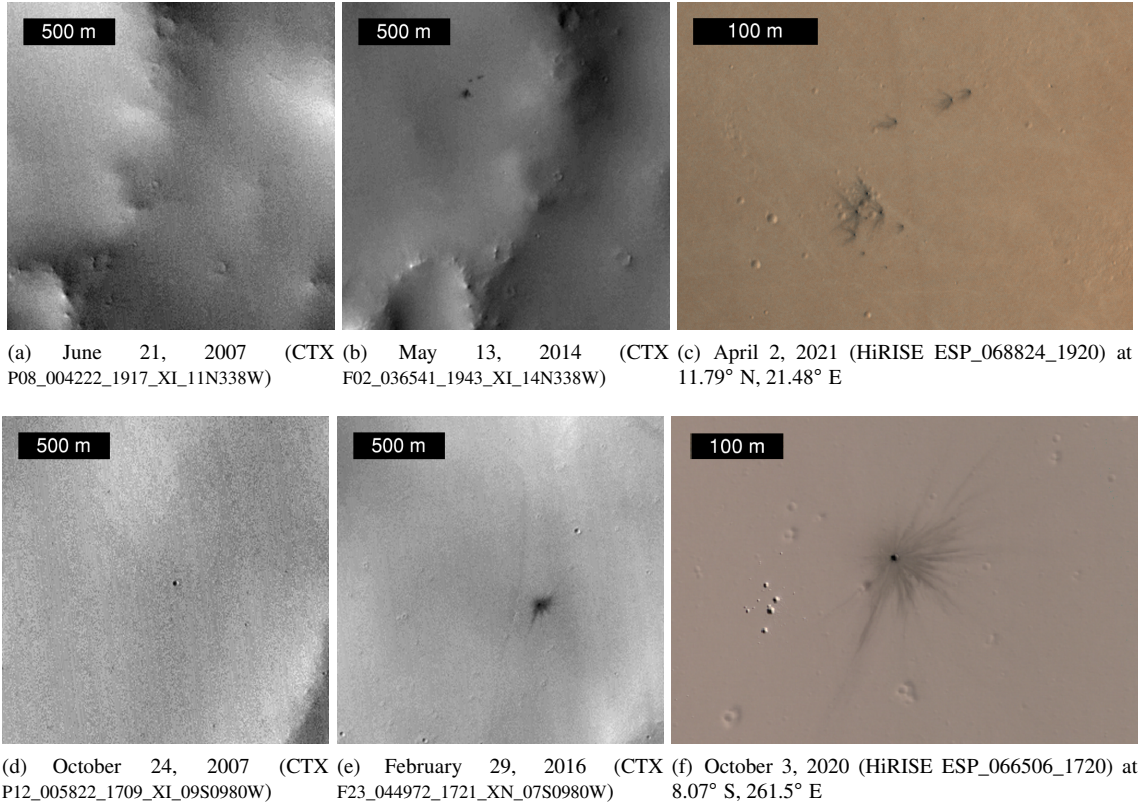


**Figure 4:** Examples of fresh impacts discovered by the machine learning classifier in CTX images: (a,d) before impact, (b,e) after impact, (c,f) follow-up image by HiRISE. Image credits: NASA/JPL/MSSS (CTX) and NASA/JPL/University of Arizona (HiRISE).

approximates the diameter that would have occurred had the impactor not fragmented in the atmosphere. The effective diameter was calculated as

$$D_{\text{eff}} = \sqrt[3]{\sum_i D_i^3}, \quad (1)$$

where  $D_i$  is the diameter of each individual crater (Malin et al., 2006; Daubar et al., 2013).

Regional characteristics were obtained from quantitative maps in JMARS using map sampling of the relevant basemap to calculate the average value within the footprint of the HiRISE image. This provides a representative value of the region, because the impacts themselves are orders of magnitude smaller than the basemap resolutions. Elevations were sampled from the MOLA 128 ppd basemap (Smith et al., 2001). Dust Cover was sampled from the TES Dust Cover Index (Ruff and Christensen, 2002). Thermal inertia was sampled from the THEMIS quantitative 100 m per pixel global mosaic (Edwards et al., 2011). Where the THEMIS data were not available, we used the average of day and night TES thermal inertia (Putzig and Mellon, 2007).

## 2.5. Review of candidates by thermal inertia

We also performed a manual review using a stratified sampling procedure that partitioned candidates by their thermal inertia values. To perform the stratified sampling of candidates, we first computed a thermal inertia value for every candidate within the detection database using the THEMIS thermal inertia map (100 m/pixel) as a primary source of measurements and using the TES map (7.5 km/pixel) as a backup as described above for manually detected candidates. In this case, we used the value of thermal inertia pixel closest to the center of the CTX window in which the candidate was found. Then, a set of 1000 candidates was obtained by selecting the top 100 candidates (by confidence)

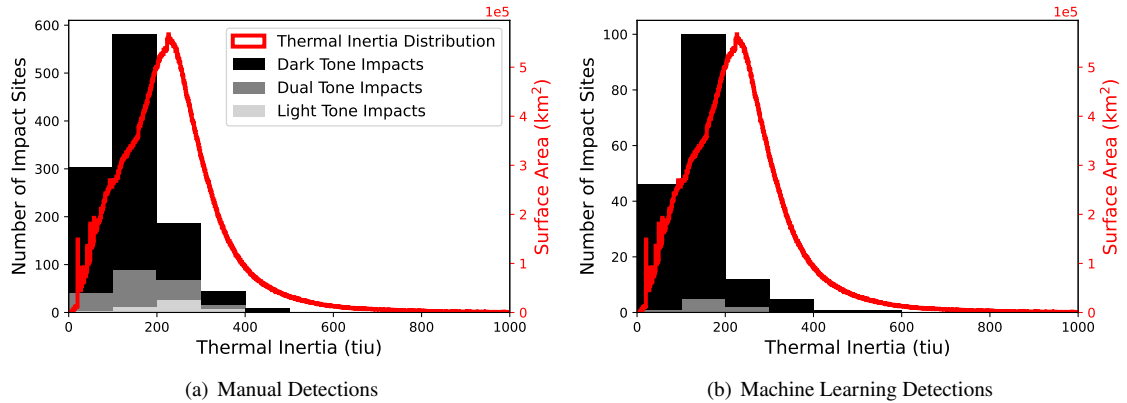


**Figure 5:** Thermal inertia distribution for fresh impacts within  $-60$  to  $60$  degrees latitude compared with the overall thermal inertia distribution for Mars over the same area, derived from TES and THEMIS thermal inertia maps. Stacked histograms show a breakdown of detections by type. The left panel shows results for manual detections, replicated from Figure 1 for direct comparison with the ML detections only (right). Both distributions show that the thermal inertia of fresh impact sites is lower than that of Mars as a whole (peak near 150 tiu vs. 225 tiu).

within each of ten thermal inertia bins evenly spaced between 0 and 1000 tiu. The review process followed the same procedure as described above.

### 3. Results and discussion

We first report on the top 1000 most-confident machine learning candidates and characterize the new discoveries, then discuss differences in candidates found by manual search versus machine learning. Finally, we report on an analysis by thermal inertia bins that helps reduce the observational bias in the catalog.

#### 3.1. Highest-confidence machine learning candidates

The manual review of the top 1000 machine learning candidates, ranked in descending order of posterior probability, yielded 169 dateable fresh impacts. Of these, 99 were already recorded in the catalog of known fresh impacts, providing confirmation of human and machine agreement. The remaining 70 dateable fresh impacts constitute the discovery of fresh impacts not previously known. An additional set of 465 candidates visually resemble fresh impacts, but the CTX archive does not contain a “before” image that pre-dates the impact’s occurrence, so the date of formation cannot be constrained. An additional 166 candidates were old or degraded impacts (not “fresh”), and 89 candidates were not impact features (e.g., mistaken with shadows due to terrain or other dark features on the surface). Because there is some imprecision in determining the location of each candidate on the surface, 111 of the top 1000 candidates were duplicates with other candidates and not automatically filtered using a distance-based threshold of 600 m.

Two examples of the fresh impacts discovered by the machine learning classifier are shown in Figure 4. The latest CTX image pre-impact and the earliest CTX image post-impact are accompanied by the follow-up image we requested from HiRISE. The first example was revealed to be a cluster of smaller impacts, while the second one is a single impact with extensive rays.

One of the primary questions driving this work was whether the machine learning candidates would exhibit the same observational bias as those identified by humans. Indeed, the most-confident machine learning candidates appear to replicate this bias and are concentrated towards areas of low thermal inertia (see Figure 5). This bias is also evident when the known impacts are plotted on a map of Mars (Figure 6). This is not surprising, since the machine learning classifier was trained on examples identified by humans; the classifier is most confident about the same kinds of impacts that it was trained on. Its ability to exhaustively search in a consistent fashion for the same kinds of features enabled the discovery of new fresh impacts that are similar to those already in the catalog. However, there are some interesting differences in the properties of the impacts that were found via machine learning compared to the pre-existing catalog.

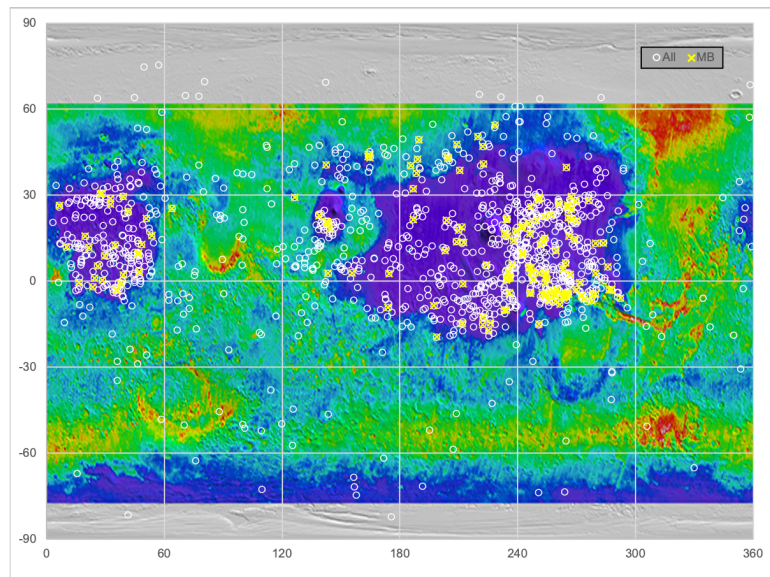
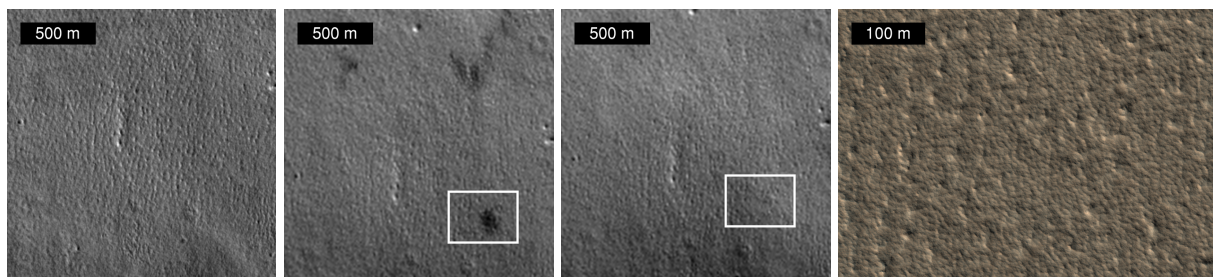


**Figure 6:** Spatial distribution of fresh impact sites on Mars overlaid on the TES thermal inertia basemap, augmented with ML-identified candidates (yellow x's).



(a) June 27, 2016 (CTX J04\_046501\_2223\_XI\_42N088W) (b) May 9, 2017 (CTX J15\_050549\_2220\_XI\_42N088W) (c) April 6, 2019 (CTX K16\_059503\_2220\_XI\_42N088W) (d) August 26, 2020 (HiRISE ESP\_066822\_2225)

**Figure 7:** Enigmatic machine learning candidate first observed on May 9, 2017 (a vs. b) that persisted through at least February 9, 2018 and disappeared by April 6, 2019 (c). A HiRISE observation acquired on August 26, 2020 revealed no visible impact at the candidate location of 43.3° N, 271.8° E (d).

### 3.2. Differences in machine learning versus manually detected candidates

Why were 70 fresh impact sites detected via machine learning but not by prior review of the CTX images? If there were no distinguishing features for these impacts, they could have been missed by random chance or due to reviewer fatigue. However, we found that there are some factors that characterize this subpopulation and could help explain how they were overlooked. These factors point to advantages of employing semi-automated search techniques.

HiRISE follow-up high-resolution images of the newly discovered impact sites were used to produce the measurements described in Section 2.4. An examination of the HiRISE images revealed that one of the 70 new fresh impacts found in CTX images did not correspond to an impact site. Features identified in low-resolution imagery are sometimes revealed to be transient or have other causes, which underscores the value of following up with HiRISE for confirmation. This site is shown in Figure 7. The dark blotches were first observed in May 2017 and persisted for at least nine Earth months (February 2018), but they are not evident in CTX or HiRISE imagery from April 2019 onward. We suspect this feature is the result of aeolian redistribution of bright dust, but cannot be certain of that explanation for this feature. As a result, we excluded this candidate and compiled measurements for 69 sites uniquely identified by the machine learning classifier and confirmed by manual review.

We compiled information about each of the 69 new discoveries, including the location (latitude, longitude) and impact properties and measurements (Table 1) and the before and after CTX images and HiRISE confirmation image (Table 2). Three of these sites were independently discovered by human review during this study. We compared the characteristics of 66 ML impacts (uniquely found by the machine learning classifier) to those of the entire catalog (including the ML impacts, 100 additional impacts that were found by both ML and humans, and 1058 previously identified impacts).

**Impact size.** The diameters of the 66 ML impact sites averaged  $5.04 \pm 2.17$  m, while the full catalog averaged  $7.22 \pm 6.09$  m. The difference in distribution of diameter values is shown in Figure 8. The full catalog has quite a few large outliers that exceed 1.5 times the inter-quartile range. This difference in distribution could indicate that ML is more effective than humans at finding the smaller impact sites (DeLatte et al., 2019; Lagain et al., 2021). It could also partially explain the previously observed difference in size-frequency distribution slope between dated martian impacts and those found on the Moon. Mars has been characterized as having relatively fewer small new impacts than the Moon, but under-counting of these small impacts was identified as a possible reason (Daubar et al., 2022). We also find that ML detects clusters more readily than they are found in the full catalog (73% of ML sites are clusters versus 59% of the full catalog). Clustered impacts may have albedo patterns that are less symmetric and more spatially dispersed, which could be easier for humans to overlook.

**Impact albedo features.** The albedo features around new impact sites are what allow us to find them in lower-resolution orbital images, so their nature is directly connected to detectability and the resulting completeness of the dataset. The most common features, halos (widespread diffuse areas of differing albedo) are similarly common among both the full catalog (88%) and the ML subset (86%). Rays (linear streaks emanating from the impact site) also have similar rates of occurrence among both groups (64% of the full catalog vs. 52% of the ML subset). The disturbed area around the impact site could be darker or lighter than the surroundings, or have some areas of dark and some areas of light. The ML sites have similar distributions between these types as the full catalog, except that dual-toned blast zones are less common among the ML sites (8% vs. 14%). This could be explained by a scarcity of dual- and light-toned impact sites in the training set, or the small numbers of these types of sites in general. (Light-toned sites are so rare, only 4% of the full catalog, that finding none in this subset is not surprising.)

**Surface characteristics.** We also explored the surface characteristics that enable detection of these new impacts to evaluate the effectiveness of ML in improving the completeness of the data. The Dust Cover Index (DCI) around the ML sites (average  $0.9361 \pm 0.0074$ ) matches closely that of the catalog as a whole ( $0.9377 \pm 0.0150$ ), and thermal inertia of the surroundings were also similar ( $142.0 \text{ Jm}^{-2}\text{K}^{-1}\text{s}^{-0.5}$  for the ML sites vs. 155.2 for the whole catalog). This demonstrates that the training set was effective at training the classifier to find impacts on the same types of terrains.

Overall, the primary distinguishing features of the ML sites were that the impacts tended to be smaller and were more likely to be composed of a cluster of impacts and therefore exhibited more variability in their spatial appearance. These impacts are likely more difficult to find using solely human review of the CTX images.

### 3.3. Fresh impacts and thermal inertia

The preceding analysis focused on the most-confident candidates identified by the machine learning classifier. Since most of the positive training examples came from areas of low thermal inertia, it is unsurprising that the most confident candidates also come from low thermal inertia areas. Our expectation is that impacts are occurring independently of the terrain type. However, impacts in high thermal inertia areas may be harder to visually detect, so if detected by the classifier, they might not be evident in the set of most confidently classified candidates.

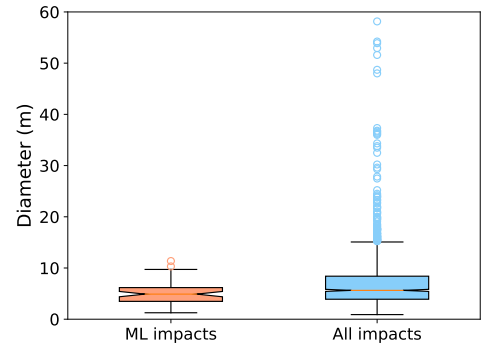
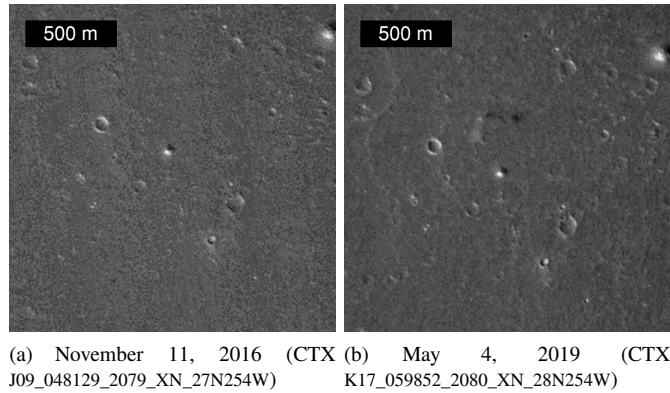


Figure 8: Distribution of fresh impact crater sizes (diameters) for impacts found uniquely by the machine learning classifier versus all impacts. The box shows the inter-quartile range (IQR or span from 25% to 75% of the distribution, whiskers extend the box by 1.5 times IQR, and outliers are shown with circles.



**Figure 9:** High thermal inertia fresh impact candidate discovered by the machine learning classifier at 27.5° N, 105.5° E.

We therefore performed a deeper search, as described in Section 2.5, to determine whether the machine learning candidates stratified by thermal inertia exhibit less bias. We divided the fresh impacts into bins based on thermal inertia and reviewed 100 candidates for each bin. This process yielded an additional five viable candidates, for which we are in the process of obtaining HiRISE follow-up images via HiWish. An example of an impact with THEMIS thermal inertia greater than 1000 tiu is shown in Figure 9. The HiRISE follow-up image, when available, will help us resolve its properties.

Figure 10 shows the distribution of impacts by their thermal inertia values (black bars) compared to the counts that would be expected given the global distribution of thermal inertia across Mars, assuming uniform observations across the surface (red hashed bars). The manually detected impacts exhibit a bias towards lower thermal inertia bins that does not match the global distribution. The most-confident machine learning detections also exhibit this bias. However, stratifying the detections by thermal inertia bin allows the detection of a larger proportion of impacts at higher thermal inertia, providing a better fit to the global distribution. Note that this strategy is possible only because the machine learning classifier generated so many candidates across the entire archive. There does not exist a similarly voluminous sample of human detections that can be stratified to reduce bias in a post-detection fashion.

To quantify the observational bias, we measure the difference between the observed ( $O$ ) and expected ( $E$ ) thermal inertia distribution of impacts using the Kullback-Leibler (KL) divergence,

$$D_{KL}(O \parallel E) = \sum_{i=1}^{10} O_i \log \frac{O_i}{E_i}, \quad (2)$$

where  $O_i$  and  $E_i$  refer to the probability of an impact occurring in thermal inertia bin  $i$ . The magnitude of  $D_{KL}(O \parallel E)$  characterizes the bias present; if the two distributions were identical, this value would be zero. The  $D_{KL}$  value for the manual detections was 0.337. The most-confident ML detections had a higher value of 0.528, while stratifying by thermal inertia corrected the bias to 0.316, a value that is lower than that of the manual detections.

Note that KL divergence naturally emphasizes differences where there is high probability mass in the distribution. In this case, it focuses on differences in the lower thermal inertia (TI) bins where most of the detections occur. The increase in detections in the highest TI bins (tiu 500-1000) obtained by the stratified method, while important scientifically, does not have as large of an influence on  $D_{KL}$ . Also, while stratification reduces some bias, other biases could remain in the data, such as biases based on the appearance of detected impacts, such as the tone of the surrounding ejecta relative to the background. A re-training of the model with additional relevant examples would be required to mitigate these appearance-based detection biases.

#### 4. Conclusions

We trained a convolutional neural network on thousands of positive and negative examples of fresh impacts and deployed it to search 112,207 images previously obtained by the Mars Reconnaissance Orbiter (MRO)'s Context Camera (CTX). After classifying more than 2 billion CTX image windows of size  $1.8 \times 1.8$  km, the top 1000 candidate

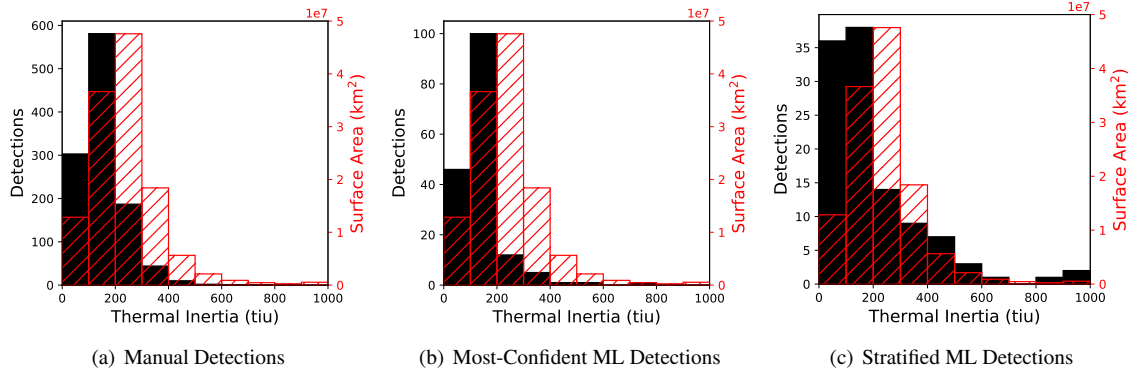


**Figure 10:** Biases in new impact crater detection rates within 60 degrees latitude from the equator for (a) human detections, (b) most-confident ML detections, and (c) thermal-inertia stratified ML detections. Black bars show impact distribution by thermal inertia. Red hashed bars show the counts expected given the Mars global thermal inertia distribution. While the most-confident ML detections replicate the manual bias, the stratification process reduces it.

detections (by classifier confidence) were manually reviewed. This process yielded 69 fresh impacts that had not been previously identified in the data. Most of the newly discovered impacts were also in low-TI regions, demonstrating consistency with the examples the model was trained on, which are primarily also in low-TI areas.

Each of the fresh impacts that were identified by the machine learning classifier were further investigated using HiRISE on MRO. The high-resolution image enabled the measurement of key impact properties such as size, multiplicity, the presence of rays, etc. During this follow-up process, three candidates were independently found by human review. We found that the properties of the 66 impacts uniquely identified by the classifier were largely consistent with those of the full catalog. However, the ML-discovered impacts were more likely to be clusters of multiple impacts, and they tended to be smaller than those in the full catalog. These impacts are therefore likely more heterogeneous and somewhat harder to detect with manual review, highlighting a useful role for the classifier in increasing coverage.

The bias towards areas of low thermal inertia in the catalog of known impacts can be addressed by assessing candidates across the TI range, not just the most confident ones. We partitioned the classifier candidates based on the thermal inertia of the terrain surrounding the candidate and reviewed the top 100 candidates for each of 10 thermal inertia ranges. This enabled the identification of five additional impacts that had not been previously found by manual detection. HiWish requests for follow-up imaging of these impacts have also been made and will enable future measurements of their properties. In addition, this analysis yielded four new discoveries of fresh impacts on terrain with thermal inertia of at least 400 tiu, a subpopulation that is rare within the catalog. This analysis was possible only because the classifier generated so many candidates across the globe, with more than one million candidates that had a posterior probability of at least 0.99.

We conclude that machine learning is a useful technique for increasing the detection of fresh impacts on Mars. The use of an automated classifier can accelerate the rate at which fresh impacts are found and catalogued. Time is still required to review the machine learning candidates, but this time is focused on the areas most likely to yield new discoveries. The classifier provides a useful pointer to focus attention where it is most likely to pay off.

## Acknowledgments

We thank Marko Green and Justin Martia for assisting with the labeling of the CTX data set, the CTX and PDS teams for providing the data, Steven Lu and Masha Liukis for developing the distributed machine learning system used to train the classifier, and the Jet Propulsion Laboratory R&TD program for funding this work. The High Performance Computing resources used in this investigation were provided by funding from the JPL Information and Technology Solutions Directorate. Part of this research was carried out at the Jet Propulsion Laboratory, California Institute of Technology, under a contract with the National Aeronautics and Space Administration. © 2021. All rights reserved.

AG, DW, JP and IJD were partially supported by NASA grant 80NSSC20K0789. VTB was supported by a fellowship within the IFI programme of the German Academic Exchange Service (DAAD).

We are grateful to the HiRISE operations team for acquiring our HiWish target suggestions in a timely manner.

## Credit authorship contribution statement

**Kiri L. Wagstaff:** Concept, Data labeling, Candidate review infrastructure, Writing. **Ingrid J. Daubar:** Initial impact catalog, Candidate review, HiRISE follow-up imaging, Measurements, Data analysis, Writing. **Gary Doran:** Globally scalable classifier deployment, Candidate database design and implementation, Experimental results, Writing. **Michael J. Munje:** Machine learning classifier training, Experimental results. **Valentin T. Bickel:** Candidate review, Analysis. **Annabelle Gao:** Candidate review, HiWish HiRISE follow-up requests, Measurements, Analysis. **Joe Pate:** Candidate review, Analysis, Writing. **Daniel Wexler:** Candidate review, HiWish HiRISE follow-up requests, Measurements.

## References

- Alexandari, A., Kundaje, A., Shrikumar, A., 2020. Maximum likelihood with bias-corrected calibration is hard-to-beat at label shift adaptation, in: Proceedings of the 2020 International Conference on Machine Learning, pp. 222–232.
- Barrett, A.M., Balme, M.R., Woods, M., Karachalios, S., Petrocelli, D., Joudrier, L., Sefton-Nash, E., 2022. NOAH-H, a deep-learning, terrain classification system for Mars: Results for the ExoMars Rover candidate landing sites. *Icarus* 371, 114701. doi:10.1016/j.icarus.2021.114701.
- Bart, G.D., Daubar, I.J., Ivanov, B.A., Dundas, C.M., McEwen, A.S., 2019. Dark halos produced by current impact cratering on Mars. *Icarus* 328, 45–57. doi:10.1016/J.ICARUS.2019.03.004.
- Bickel, V.T., Aaron, J., Manconi, A., Loew, S., Mall, U., 2020a. Impacts drive lunar rockfalls over billions of years. *Nature Communications* doi:10.1038/s41467-020-16653-3.
- Bickel, V.T., Conway, S.J., Tesson, P.A., Manconi, A., Loew, S., Mall, U., 2020b. Deep learning-driven detection and mapping of rockfalls on Mars. *IEEE Journal of Selected Topics in Applied Earth Observations and Remote Sensing* 13, 2831–2841. doi:10.1109/JSTARS.2020.2991588.
- Burleigh, K.J., Melosh, H.J., Tornabene, L.L., Ivanov, B., McEwen, A.S., Daubar, I.J., 2012. Impact airblast triggers dust avalanches on Mars. *Icarus* 217, 194–201. doi:10.1016/j.icarus.2011.10.026.
- Byrne, S., Dundas, C.M., Kennedy, M.R., Mellon, M.T., McEwen, A.S., Cull, S.C., Daubar, I.J., Shean, D.E., Seelos, K.D., Murchie, S.L., Cantor, B.A., Arvidson, R.E., Edgett, K.S., Reufer, A., Thomas, N., Harrison, T.N., Posiolova, L.V., Seelos, F.P., 2009. Distribution of mid-latitude ground ice on Mars from new impact craters. *Science* 325, 1674–1676. doi:10.1126/science.1175307.
- Chojnacki, M., McEwen, A.S., Byrne, S., Hansen, C., Daubar, I.J., Beyer, R., McArthur, G., the HiRISE science, operations team, 2020. HiWish: The High Resolution Imaging Science Experiment (HiRISE) suggestion tool, in: Proceedings of the 51st Lunar and Planetary Science Conference, The Woodlands, TX. Abstract 2095.
- Christensen, P.R., Bandfield, J.L., Hamilton, V.E., Ruff, S.W., Kieffer, H.H., Titus, T.N., Malin, M.C., Morris, R.V., Lane, M.D., Clark, R.L., Jakosky, B.M., Mellon, M.T., Pearl, J.C., Conrath, B.J., Smith, M.D., Clancy, R.T., Kuzmin, R.O., Roush, T., Mehall, G.L., Gorelick, N., Bender, K., Murray, K., Dason, S., Greene, E., Silverman, S., Greenfield, M., 2001. Mars Global Surveyor Thermal Emission Spectrometer experiment: Investigation description and surface science results. *Journal of Geophysical Research: Planets* 106, 23823–23871. doi:10.1029/2000JE001370.
- Christensen, P.R., Engle, E., Anwar, S., Dickensied, S., Noss, D., Gorelick, N., Weiss-Malik, M., 2009. JMARS - A planetary GIS, in: Proceedings of the Fall Meeting of the AGU, pp. Abstract IN22A–06.
- Christensen, P.R., Jakosky, B.M., Kieffer, H.H., Malin, M.C., Jr., H.Y.M., Neelson, K., Mehall, G.L., Silverman, S.H., Ferry, S., Caplinger, M., Ravine, M., 2004. The Thermal Emission Imaging System (THEMIS) for the Mars 2001 Odyssey mission. *Space Science Reviews* 110, 85–130. doi:10.1023/B:SPAC.0000021008.16305.94.
- Daubar, I., Dundas, C., Byrne, S., Geissler, P., Bart, G., McEwen, A., Russell, P., Chojnacki, M., Golombek, M., 2016. Changes in blast zone albedo patterns around new martian impact craters. *Icarus* 267, 86–105. doi:10.1016/j.icarus.2015.11.032.
- Daubar, I.J., Atwood-Stone, C., Byrne, S., McEwen, A.S., Russell, P.S., 2014. The morphology of small fresh craters on Mars and the moon. *Journal of Geophysical Research: Planets* 119, 2620–2639. doi:10.1002/2014JE004671.
- Daubar, I.J., Banks, M.E., Schmerr, N.C., Golombek, M.P., 2019. Recently formed crater clusters on Mars. *Journal of Geophysical Research: Planets* 124, 958–969. doi:10.1029/2018JE005857.
- Daubar, I.J., Dundas, C., McEwen, A.S., Gao, A., Wexler, D., Piqueux, S., Collins, G.S., Mijakovic, K., Neidhart, T., Eschenfelder, J., Bart, G.D., Wagstaff, K., Doran, G., Posiliova, L., Malin, M., 2022. New craters on Mars: An updated catalog. *Journal of Geophysical Research: Planets* doi:10.1029/2021JE007145.
- Daubar, I.J., Gao, A., Wexler, D., Dundas, C., McEwen, A., Neidhart, T., Mijakovic, K., Eschenfelder, J., Collins, G.S., Piqueux, S., Malin, M., Posiolova, L., 2020. New craters on Mars: An updated catalog, in: Proceedings of the 11th Planetary Crater Consortium. Abstract 2069.
- Daubar, I.J., McEwen, A.S., Byrne, S., Kennedy, M.R., Ivanov, B., 2013. The current martian cratering rate. *Icarus* 225, 506–516. doi:10.1016/j.icarus.2013.04.009.
- DeLatte, D., Crites, S., Guttenberg, N., Yairi, T., 2019. Automated crater detection algorithms from a machine learning perspective in the convolutional neural network era. *Advances in Space Research* 64, 1615–1628. URL: <https://www.sciencedirect.com/science/article/pii/S0273117719305071>. doi:<https://doi.org/10.1016/j.asr.2019.07.017>.
- Dundas, C.M., Byrne, S., McEwen, A.S., Mellon, M.T., Kennedy, M.R., Daubar, I.J., Saper, L., 2014. HiRISE observations of new impact craters exposing Martian ground ice. *Journal of Geophysical Research: Planets* 119, 109–127. doi:10.1002/2013JE004482.

- Dundas, C.M., Mellon, M.T., Conway, S.J., Daubar, I.J., Williams, K.E., Ojha, L., Wray, J.J., Bramson, A.M., Byrne, S., McEwen, A.S., Posiolova, L.V., Speth, G., Viola, D., Landis, M.E., Morgan, G.A., Pathare, A.V., 2021. Widespread exposures of extensive clean shallow ice in the midlatitudes of Mars. *Journal of Geophysical Research: Planets* 126, e2020JE006617. doi:10.1029/2020JE006617.
- Edwards, C.S., Nowicki, K.J., Christensen, P.R., Hill, J., Gorelick, N., Murray, K., 2011. Mosaicking of global planetary image datasets: 1. Techniques and data processing for Thermal Emission Imaging System (THEMIS) multi-spectral data. *Journal of Geophysical Research: Planets* 116. doi:10.1029/2010JE003755.
- Hartmann, W.K., 2005. Martian cratering 8: Isochron refinement and the chronology of Mars. *Icarus* 174, 294–320.
- Hartmann, W.K., Daubar, I.J., 2017. Martian cratering 11. Utilizing decameter scale crater populations to study Martian history. *Meteoritics & Planetary Science* 52, 493–510. doi:10.1111/maps.12807.
- Hartmann, W.K., Neukum, G., 2001. Cratering chronology and the evolution of Mars. *Space Science Reviews* 96, 165–194.
- Ivanov, B.A., 2001. Mars/Moon cratering rate ratio estimates. *Space Science Reviews* 96, 87–104.
- Jia, Y., Liu, L., Zhang, C., 2021. Moon impact crater detection using nested attention mechanism based unet++. *IEEE Access* 9, 44107–44116. doi:10.1109/ACCESS.2021.3066445.
- Kerner, H.R., Wagstaff, K.L., Bue, B.D., Wellington, D.F., Jacob, S., Horton, P., III, J.F.B., Kwan, C., Amor, H.B., 2020. Comparison of novelty detection methods for multispectral images in rover-based planetary exploration missions. *Data Mining and Knowledge Discovery* 34, 1642–1675. doi:10.1007/s10618-020-00697-6.
- Kodikara, G.R., McHenry, L.J., 2020. Machine learning approaches for classifying lunar soils. *Icarus* 345, 113719. doi:10.1016/j.icarus.2020.113719.
- Lagain, A., Servis, K., Benedix, G.K., Norman, C., Anderson, S., Bland, P.A., 2021. Model age derivation of large Martian impact craters, using automatic crater counting methods. *Earth and Space Science* 8, e2020EA001598. URL: <https://agupubs.onlinelibrary.wiley.com/doi/abs/10.1029/2020EA001598>, doi:https://doi.org/10.1029/2020EA001598.
- Malin, M.C., Bell III, J.F., Cantor, B.A., Caplinger, M.A., Calvin, W.M., Clancy, R.T., Edgett, K.S., Edwards, L., Haberle, R.M., James, P.B., Lee, S.W., Ravine, M.A., Thomas, P.C., Wolff, M.J., 2007. Context Camera Investigation on board the Mars Reconnaissance Orbiter. *Journal of Geophysical Research: Planets* 112. doi:10.1029/2006JE002808.
- Malin, M.C., Edgett, K.S., Posiolova, L.V., McColley, S.M., Dobrea, E.Z.N., 2006. Present-day impact cratering rate and contemporary gully activity on Mars. *Science* 314, 1573–1577. doi:10.1126/science.1135156.
- McEwen, A.S., Eliason, E.M., Bergstrom, J.W., Bridges, N.T., Hansen, C.J., Delamere, W.A., Grant, J.A., Gulick, V.C., Herkenhoff, K.E., Keszthelyi, L., Kirk, R.L., Mellon, M.T., Squyres, S.W., Thomas, N., Weitz, C.M., 2007. Mars Reconnaissance Orbiter's High Resolution Imaging Science Experiment (HiRISE). *Journal of Geophysical Research: Planets* 112. doi:10.1029/2005JE002605.
- Naeni, M.P., Cooper, G.F., Hauskrecht, M., 2015. Obtaining well calibrated probabilities using bayesian binning, in: *Proceedings of the... AAAI Conference on Artificial Intelligence*. AAAI Conference on Artificial Intelligence, NIH Public Access. p. 2901.
- Ono, M., Rothrock, B., Almeida, E., Ansar, A., Otero, R., Huertas, A., Heverly, M., 2016. Data-driven surface traversability analysis for Mars 2020 landing site selection, in: *2016 IEEE Aerospace Conference*, pp. 1–12. doi:10.1109/AERO.2016.7500597.
- Palafox, L.F., Hamilton, C.W., Scheidt, S.P., Alvarez, A.M., 2017. Automated detection of geological landforms on Mars using Convolutional Neural Networks. *Computers & Geosciences* 101, 48–56. doi:10.1016/j.cageo.2016.12.015.
- Paszke, A., Gross, S., Massa, F., Lerer, A., Bradbury, J., Chanan, G., Killeen, T., Lin, Z., Gimelshein, N., Antiga, L., Desmaison, A., Kopf, A., Yang, E., DeVito, Z., Raison, M., Tejani, A., Chilamkurthy, S., Steiner, B., Fang, L., Bai, J., Chintala, S., 2019. Pytorch: An imperative style, high-performance deep learning library, in: *Wallach, H., Larochelle, H., Beygelzimer, A., d'Alché-Buc, F., Fox, E., Garnett, R. (Eds.), Advances in Neural Information Processing Systems 32*. Curran Associates, Inc., pp. 8024–8035. URL: <http://papers.neurips.cc/paper/9015-pytorch-an-imperative-style-high-performance-deep-learning-library.pdf>.
- Putzig, N.E., Mellon, M.T., 2007. Apparent thermal inertia and the surface heterogeneity of Mars. *Icarus* 191, 68–94. doi:10.1016/j.icarus.2007.05.013.
- Robbins, S.J., Hynes, B.M., 2012. A new global database of Mars impact craters  $\geq 1$  km: 1. database creation, properties, and parameters. *Journal of Geophysical Research: Planets* 117. doi:10.1029/2011JE003966.
- Ruff, S.W., Christensen, P.R., 2002. Bright and dark regions on Mars: Particle size and mineralogical characteristics based on Thermal Emission Spectrometer data. *Journal of Geophysical Research: Planets* 107, 10–1–10–22. doi:10.1029/2000JE001364.
- Russakovsky, O., Deng, J., Su, H., Krause, J., Satheesh, S., Ma, S., Huang, Z., Karpathy, A., Khosla, A., Bernstein, M., Berg, A.C., Fei-Fei, L., 2015. ImageNet Large Scale Visual Recognition Challenge. *International Journal of Computer Vision (IJCV)* 115, 211–252. doi:10.1007/s11263-015-0816-y.
- Silburt, A., Ali-Dib, M., Zhu, C., Jackson, A., Valencia, D., Kissin, Y., Tamayo, D., Menou, K., 2019. Lunar crater identification via deep learning. *Icarus* 317, 27–38. URL: <https://www.sciencedirect.com/science/article/pii/S0019103518301386>, doi:https://doi.org/10.1016/j.icarus.2018.06.022.
- Smith, D.E., Zuber, M.T., Frey, H.V., Garvin, J.B., Head, J.W., Muhleman, D.O., Pettengill, G.H., Phillips, R.J., Solomon, S.C., Zwally, H.J., Banerdt, W.B., Duxbury, T.C., Golombek, M.P., Lemoine, F.G., Neumann, G.A., Rowlands, D.D., Aharonson, O., Ford, P.G., Ivanov, A.B., Johnson, C.L., McGovern, P.J., Abshire, J.B., Afzal, R.S., Sun, X., 2001. Mars Orbiter Laser Altimeter: Experiment summary after the first year of global mapping of Mars. *Journal of Geophysical Research: Planets* 106, 23689–23722. doi:10.1029/2000JE001364.
- Szegedy, C., Liu, W., Jia, Y., Sermanet, P., Reed, S., Anguelov, D., Erhan, D., Vanhoucke, V., Rabinovich, A., 2015. Going deeper with convolutions, in: *Proceedings of the IEEE Conference on Computer Vision and Pattern Recognition (CVPR)*. doi:10.1109/CVPR.2015.7298594.
- Viviano, C.E., Murchie, S.L., Daubar, I.J., Morgan, M.F., Seelos, F.P., Plescia, J.B., 2019. Composition of Amazonian volcanic materials in Tharsis and Elysium, Mars, from MRO/CRISM reflectance spectra. *Icarus* 328, 274–286. doi:10.1016/j.icarus.2019.03.001.
- Wagstaff, K., Lu, S., Dunkel, E., Grimes, K., Zhao, B., Cai, J., Cole, S.B., Doran, G., Francis, R., Lee, J., Mandrake, L., 2021. Mars image content classification: Three years of NASA deployment and recent advances, in: *Proceedings of the Thirty-Third Annual Conference on Innovative Applications of Artificial Intelligence*, pp. 15204–15213.

## Using Machine Learning to Reduce Observational Biases When Detecting New Impacts on Mars

- Wagstaff, K.L., Lu, Y., Stanboli, A., Grimes, K., Gowda, T., Padams, J., 2018. Deep Mars: CNN classification of Mars imagery for the PDS Imaging Atlas, in: Proceedings of the Thirtieth Annual Conference on Innovative Applications of Artificial Intelligence, pp. 7867–7872.
- Wilhelm, T., Geis, M., Püttschneider, J., Sievernich, T., Weber, T., Wohlfarth, K., Wöhler, C., 2020. DoMars16k: A diverse dataset for weakly supervised geomorphologic analysis on Mars. Remote Sensing 12. URL: <https://www.mdpi.com/2072-4292/12/23/3981>, doi:10.3390/rs12233981.
- Williams, J.P., Pathare, A.V., Aharonson, O., 2014. The production of small primary craters on Mars and the Moon. Icarus 235, 23–36. doi:10.1016/j.icarus.2014.03.011.

**Table 1**

Location and properties of fresh impacts discovered via machine learning, sorted by thermal inertia.

Id	Latitude (N)	Longitude (E)	Type	Halo?	Rays?	Effective diameter	Dust cover index	Thermal inertia
1	9.1990	242.6790	cluster	y	y	7.41	0.9369	44.91
2	39.6142	264.8912	cluster	y	n	6.29	0.9218	45.14
3	-6.1622	274.1629	cluster	y	n	2.64	0.9348	60.66
4	-3.0650	287.9550	single	n	n	4.50	0.9448	63.82
5	-14.5268	225.9985	cluster	y	y	7.88	0.9382	74.78
6	29.5490	39.0180	single	y	n	3.26	0.9260	75.56
7	30.3690	27.3720	cluster	y	n	3.17	0.9254	79.27
8	23.3190	257.0400	cluster	y	y	4.97	0.9260	80.80
9	-4.8700	253.9290	cluster	y	n	9.06	0.9384	83.49
10	11.8900	10.0560	single	y	y	2.88	0.9322	84.97
11	-5.8643	292.3527	cluster	y	n	3.33	0.9441	87.10
12	1.7600	254.4290	single	y	y	5.67	0.9315	88.62
13	0.6796	255.0087	cluster	y	n	5.85	0.9317	90.05
14	8.9010	29.6060	cluster	y	y	4.34	0.9385	91.43
15	-4.3845	279.6718	single	y	n	2.75	0.9446	92.94
16	-4.2270	256.5710	cluster	y	n	9.72	0.9349	96.07
17	22.55271	253.8839	cluster	y	y	5.66	0.9354	99.41
18	-0.4373	16.4684	cluster	y	n	4.64	0.9467	100.37
19	-2.859	259.977	cluster	n	y	9.17	0.9406	100.67
20	12.7930	48.4590	single	y	y	3.83	0.9346	101.01
21	-4.4959	264.2976	cluster	y	y	4.99	0.9372	102.31
22	-5.8110	263.4880	cluster	n	n	7.08	0.9484	104.50
23	29.0800	251.0380	cluster	n	y	4.81	0.9274	108.49
24	-1.9970	23.5660	single	y	y	4.11	0.9456	109.37
25	21.3150	249.4010	cluster	y	y	5.31	0.9319	110.57
26	2.6430	174.4250	single	y	n	1.26	0.9312	114.37
27	2.8903	254.1615	cluster	y	y	11.36	0.9301	116.43
28	16.6122	246.3148	cluster	n	y	10.31	0.9342	125.21
29	40.4860	142.3931	single	y	n	4.90	0.9405	126.44
30	-3.9690	235.9680	single	y	y	5.00	0.9358	129.60
31	43.5112	163.9189	single	n	n	2.30	0.9435	129.78
32	12.762	251.467	single	n	y	3.63	0.9379	131.16
33	-0.4776	271.6420	cluster	y	y	4.05	0.9327	131.25
34	2.9980	247.4600	single	y	n	4.98	0.9428	131.59
35	-4.1960	262.5030	cluster	y	y	5.67	0.9389	132.86
36	-8.0650	261.4580	single	y	y	2.37	0.9432	133.25
37	20.8956	142.5618	cluster	y	n	6.64	0.9356	133.86
38	-14.8476	250.9032	cluster	n	n	3.74	0.9552	136.46
39	-4.6036	264.0991	cluster	y	y	5.75	0.9364	137.27
40	0.3060	28.4810	cluster	y	n	4.42	0.9473	139.08
41	-2.9244	270.0695	single	y	n	2.25	0.9423	140.54
42	20.6012	142.8866	single	y	y	3.70	0.9278	142.74
43	21.5430	267.2350	cluster	y	n	7.25	0.9283	143.87
44	-4.9936	259.1517	cluster	y	y	5.19	0.9433	148.18
45	-0.6070	254.0170	cluster	n	n	8.51	0.9341	148.48
46	2.7460	279.8160	single	y	y	2.84	0.9409	148.97
47	-6.8390	277.7210	cluster	y	n	5.38	0.9480	150.71
48	-4.4870	258.6750	cluster	y	y	6.34	0.9319	151.02
49	47.6020	209.0360	cluster	y	n	4.73	0.9337	151.63
50	-6.7113	255.7250	cluster	n	n	9.07	0.9519	154.55
51	27.0131	260.7333	cluster	y	n	4.91	0.9262	161.00
52	26.8140	32.5150	cluster	y	y	1.94	0.9237	163.99
53	-4.4250	254.3330	cluster	y	n	7.15	0.9353	164.55
54	2.8290	155.6070	single	y	n	1.50	0.9319	167.59
55	13.20978	279.55647	cluster	y	y	3.76	0.9454	167.65
56	-0.9353	212.0407	cluster	y	n	6.28	0.9369	175.90
57	25.9570	246.6694	cluster	y	y	6.81	0.9320	176.46
58	18.8686	211.5511	cluster	y	n	4.90	0.9305	177.76
59	10.6180	259.5470	cluster	y	y	5.64	0.9384	183.64
60	11.7909	21.4820	cluster	n	y	4.08	0.9346	201.62
61	-10.0940	233.1460	cluster	y	y	4.37	0.9335	213.04
62	24.2920	41.5100	cluster	y	y	4.11	0.9309	215.12
63	15.84881	53.525	cluster	y	n	2.45	0.9362	217.94
64	-3.2060	35.4300	cluster	y	y	3.27	0.9440	227.34
65	13.646	252.922	single	n	n	3.67	0.9367	228.22
66	28.4210	250.4310	cluster	y	y	5.55	0.9190	315.92
67	21.8120	50.8230	single	y	n	2.27	0.9374	324.99
68	26.3710	6.5540	cluster	y	y	3.41	0.9263	346.44
69	25.8970	265.3760	cluster	y	y	7.96	0.9325	394.27

Table 2

CTX before/after images and HiRISE confirmation images for fresh impacts discovered via machine learning, sorted by thermal inertia. Latitude is in degrees north and longitude is in degrees east.

Id	Latitude	Longitude	CTX before	Date	CTX after	Date	HiRISE image
1	9.1990	242.6790	P18 008064 1868 XN 06N117W	2008-04-15	J04 046344 1906 XI 10N117W	2016-06-15	ESP 066533 1895
2	39.6142	264.8912	B20 017280 2195 XN 39N095W	2010-04-03	F03 036822 2191 XN 39N095W	2014-06-04	ESP 067007 2200
3	-6.1622	274.1629	P17 007496 1738 XI 06S086W	2008-03-02	G14 023873 1727 XN 07S085W	2011-08-30	ESP 072283 1740
4	-3.0650	287.9550	F04 037428 1779 XN 02S072W	2014-07-21	J02 045459 1770 XN 03S071W	2016-04-07	ESP 070252 1770
5	-14.5268	225.9985	F03 036916 1674 XI 12S134W	2014-06-12	K02 054032 1674 XN 12S134W	2018-02-04	ESP 068315 1655
6	29.5490	39.0180	B20 017407 2108 XN 30N321W	2010-04-13	J03 045969 2118 XN 31N321W	2016-05-17	ESP 066857 2100
7	30.3690	27.3720	B07 012423 2099 XN 29N332W	2009-03-21	F03 036923 2096 XN 29N332W	2014-06-12	ESP 067781 2105
8	23.3190	257.0400	P22 009607 1715 XI 08S127W	2008-08-14	K12 057896 1705 XN 09S127W	2018-12-02	ESP 066915 2035
9	-4.8700	253.9290	B18 016740 1742 XN 05S106W	2010-02-20	J12 049561 1737 XI 06S105W	2017-02-21	ESP 067377 1750
10	11.8900	10.0560	G07 020797 1918 XI 11N349W	2011-01-03	J07 047592 1917 XN 11N350W	2016-09-20	ESP 067122 1920
11	-5.8643	292.3527	D02 028158 1732 XI 06S067W	2012-07-29	D20 034896 1724 XI 07S067W	2014-01-05	ESP 069764 1740
12	1.7600	254.4290	G04 019972 1991 XI 19N148W	2010-10-30	K04 054995 1990 XN 19N148W	2018-04-20	ESP 067720 1820
13	0.6796	255.0087	P16 007233 1808 XN 00N104W	2008-02-11	K11 057816 1799 XN 00S105W	2018-11-26	ESP 070029 1805
14	8.9010	29.6060	P17 007584 1915 XI 11N330W	2008-03-09	D16 033442 1915 XI 11N330W	2013-09-14	ESP 067306 1890
15	-4.3845	279.6718	P17 007654 1730 XN 07S080W	2008-03-14	J04 046501 1730 XN 07S080W	2016-06-27	ESP 068907 1755
16	-4.2270	256.5710	F05 037706 1761 XI 03S103W	2014-08-12	K10 057196 1739 XN 06S103W	2018-10-09	ESP 067179 1755
17	22.55271	253.8839	D18 034238 2026 XN 22N106W	2013-11-15	K17 059873 2046 XI 24N106W	2019-05-05	ESP 069607 2030
18	-0.4373	16.4684	B02 010261 1786 XI 01S343W	2008-10-04	F23 044704 1797 XN 00S343W	2016-02-08	ESP 066792 1795
19	-2.859	259.977	P20 008683 1754 XN 04S099W	2008-06-03	J19 052132 1754 XI 04S099W	2017-09-09	ESP 065644 1770
20	12.7930	48.4590	G14 023802 1932 XN 13N311W	2011-08-25	D15 033072 1950 XN 15N311W	2013-08-16	ESP 067556 1930
21	-4.4959	264.2976	P17 007615 1764 XN 03S096W	2008-03-11	B18 016555 1759 XN 04S095W	2010-02-06	ESP 068406 1755
22	-5.8110	263.4880	F19 043073 1745 XN 05S096W	2015-10-04	K05 055402 1716 XI 08S096W	2018-05-22	ESP 067469 1740
23	29.0800	251.0380	P04 002763 2080 XN 28N109W	2007-02-27	P11 005453 2080 XN 28N108W	2007-09-25	ESP 067245 2095
24	-1.9970	23.5660	B02 010419 1771 XI 02S336W	2008-10-16	K06 055569 1756 XI 04S336W	2018-06-04	ESP 067491 1780
25	21.3150	249.4010	P04 002473 2019 XN 21N110W	2007-02-05	J01 045368 2032 XN 23N110W	2016-03-31	ESP 067034 2015
26	2.6430	174.4250	D02 028004 1840 XN 04N185W	2012-07-17	F20 043630 1858 XN 05N185W	2015-11-17	ESP 066773 1825
27	2.8903	254.1615	P18 008235 1828 XI 02N106W	2008-04-29	K12 058093 1807 XN 00N105W	2018-12-18	ESP 066902 1830
28	16.6122	246.3148	P03 002183 1972 XI 17N113W	2007-01-13	P12 005717 1973 XI 17N113W	2007-10-15	ESP 066480 1970
29	40.8660	142.3931	G22 026739 2235 XN 43N218W	2012-04-10	D20 034954 2216 XN 41N217W	2014-01-10	ESP 069334 2210
30	-3.9690	235.9680	G22 026683 1749 XI 05S124W	2012-04-05	K05 055337 1784 XN 01S124W	2018-05-17	ESP 069278 1760
31	43.5112	163.9189	D07 029758 2236 XN 43N195W	2012-12-01	D15 033239 2214 XI 41N195W	2013-08-29	ESP 069320 2240
32	12.7612	251.467	P20 008881 1913 XN 11N108W	2008-06-18	F05 037627 1917 XN 11N108W	2014-08-06	ESP 065517 1930
33	-0.4776	271.6420	G04 019693 1786 XN 01S088W	2010-10-08	K05 055283 1786 XN 01S088W	2018-05-13	ESP 067627 1795
34	2.9980	247.4600	P05 002816 1820 XI 02N112W	2007-03-03	D02 028120 1842 XI 04N112W	2012-07-26	ESP 066612 1830
35	-4.1960	262.5030	G21 026537 1784 XN 01S097W	2012-03-25	K22 061996 1784 XI 01S097W	2019-10-18	ESP 067126 1760
36	-8.0650	261.4580	P15 006890 1717 XN 08S098W	2008-01-15	F23 044972 1721 XN 07S098W	2016-02-29	ESP 066506 1720
37	20.8956	142.5618	P11 005457 2016 XI 21N217W	2007-09-25	K13 058387 2015 XI 21N217W	2019-01-10	ESP 069466 2010
38	-14.8476	250.9032	P17 007576 1672 XI 12S109W	2008-03-08	B03 010714 1652 XI 14S109W	2008-11-08	ESP 069172 1650
39	-4.6036	264.0991	P17 007615 1764 XN 03S096W	2008-03-01	F21 043996 1763 XI 03S096W	2015-12-15	ESP 068010 1755
40	0.3060	28.4810	B05 011566 1800 XI 00N331W	2009-01-13	K11 057666 1787 XI 01S331W	2018-11-14	ESP 067438 1805
41	-2.9244	270.0695	B09 013034 1786 XN 01S090W	2009-05-08	K12 058132 1766 XN 03S090W	2018-12-21	ESP 068287 1770
42	20.6012	142.8866	G05 020291 2008 XN 20N217W	2010-11-24	G13 023126 2009 XN 20N217W	2011-07-03	ESP 070389 2010
43	21.5430	267.2350	F16 041886 2016 XI 21N092W	2015-07-04	K15 059134 2016 XI 21N092W	2019-03-09	ESP 066598 2020
44	-4.9936	259.1517	B02 010384 1754 XI 04S101W	2008-10-13	J10 048585 1729 XI 07S100W	2016-12-07	ESP 067997 1750
45	-0.6070	254.0170	P07 003752 1796 XN 00S105W	2007-05-15	P21 009237 1800 XI 00N106W	2008-07-16	ESP 067311 1795
46	2.7460	279.8160	P08 004173 1812 XI 01N080W	2007-06-17	J05 046791 1808 XI 00N079W	2016-07-20	ESP 067310 1830
47	-6.8390	277.7210	B02 010568 1726 XN 07S082W	2008-10-27	D04 028897 1729 XN 07S082W	2012-09-25	ESP 028897 1730
48	-4.4870	258.6750	G09 021856 1765 XN 03S101W	2011-03-26	J10 048875 1730 XI 07S101W	2016-12-29	ESP 067390 1755
49	47.6020	209.0360	P20 008711 2286 XN 48N151W	2008-06-05	D22 035624 2280 XN 48N151W	2014-03-03	ESP 066943 2280
50	-6.7113	255.7250	B01 010160 1757 XI 04S104W	2008-09-26	J21 052831 1730 XI 07S104W	2017-11-03	ESP 070385 1730
51	27.0131	260.7333	P17 007760 2069 XN 26N099W	2008-03-23	G21 026471 2073 XN 27N099W	2012-03-20	ESP 069910 2075
52	26.8140	32.5150	G21 026453 2074 XN 27N327W	2012-03-18	K23 062558 2073 XI 27N327W	2019-12-01	ESP 067319 2075
53	-4.4250	254.3330	G09 021632 1756 XN 04S105W	2011-03-09	F06 038049 1754 XN 04S105W	2014-09-08	ESP 066968 1755
54	2.8290	155.6070	P15 006762 1831 XI 03N204W	2008-01-05	D18 034123 1816 XN 01N204W	2013-11-06	ESP 067341 1830
55	13.20978	279.55647	B17 016317 1920 XN 12N080W	2010-01-18	J05 046580 1938 XN 13N080W	2016-07-04	ESP 069738 1935
56	-0.9353	212.0407	P14 006694 1776 XN 02S147W	2010-12-31	K04 055061 1773 XN 02S147W	2018-04-25	ESP 069081 1790
57	25.9570	246.6694	P02 001761 2054 XN 25N113W	2006-12-11	G05 020274 2069 XN 26N113W	2010-11-23	ESP 067641 2060
58	18.8686	211.5511	G04 019972 1991 XI 19N148W	2010-10-30	K04 054995 1990 XN 19N148W	2018-04-20	ESP 068355 1990
59	10.6180	259.5470	B18 016832 1895 XI 09N100W	2010-02-28	J10 048809 1925 XI 12N100W	2016-12-24	ESP 067192 1905
60	11.7909	21.4820	P08 004222 1917 XI 11N338W	2007-06-21	F02 036541 1943 XI 14N338W	2014-05-13	ESP 068824 1920
61	-10.0940	233.1460	P22 009607 1715 XI 08S127W	2008-08-14	K12 057896 1705 XN 09S127W	2018-12-02	ESP 066916 1700
62	24.2920	41.5100	F05 037661 2046 XN 24N318W	2014-08-09	J15 050452 2046 XI 24N318W	2017-05-01	ESP 067543 2045
63	15.84881	53.525	G11 005368 1967 XN 16N306W	2007-09-18	K03 054592 1963 XN 16N306W	2018-03-20	ESP 069588 1960
64	-3.2060	35.4300	P22 009607 1715 XN 08S127W	2012-04-04	J18 051982 1764 XI 03S324W	2017-08-28	ESP 066633 1770
65	13.646	252.922	B19 016885 1951 XI 15N107W	2010-03-04	K04 055099 1913 XN 11N106W	2018-04-28	ESP 065385 1940
66	28.4210	250.4310	P07 003752 2085 XN 28N109W	2007-05-15	F17 042414 2075 XI 27N109W	2015-08-14	ESP 066559 2085
67	21.8120	50.8230	F02 036764 2018 XN 21N309W	2014-05-31	K04 055080 2045 XN 24N309W	2018-04-27	ESP 066883 2020
68	26.3710	6.5540	B08 012938 2091 XN 29N353W	2009-04-30	J22 033552 2064 XI 26N353W	2017-12-29	ESP 066502 2065
69	25.8970	265.3760	P13 006270 2064 XN 26N094W	2007-11-28	J15 050457 2070 XI 27N094W	2017-05-02	ESP 067073 2060